

Classification of topological phase transitions and van Hove singularity steering mechanism in graphene superlattices

Jian Wang¹ and Luiz H. Santos¹

¹*Department of Physics, Emory University, Atlanta, Georgia 30322, USA*

(Dated: April 17, 2022)

We study quantum phase transitions in graphene superlattices in external magnetic field, where a framework is presented to classify multi-flavor Dirac fermion critical points describing hopping-tuned topological phase transitions of integer and fractional Hofstadter-Chern insulators. We argue and provide numerical support for the existence of transitions that can be explained by a non-trivial interplay of Chern bands and van Hove singularities near charge neutrality. This work provides a route to critical phenomena beyond conventional quantum Hall plateau transitions.

Electronic Chern bands[1, 2] are the building blocks of the Hofstadter spectrum[3] when a large magnetic flux (of order $\phi_0 = h/e$) penetrates the unit cell of the 2D lattice. They give rise to quantum Hall phases beyond the Landau level paradigm, which have attracted considerable interest.[4–8] Rapid progress in the fabrication of superlattices with nanometer scale unit cells has led to the experimental realization of integer[9–12] and fractional[13] Hofstadter-Chern insulators (IHCI and FHCI), thereby opening remarkable prospects to explore the non-trivial interplay of lattice effects and electronic topology that is inaccessible in regular 2D lattices.

Topological ground states supported in Chern bands have been broadly studied using different approaches including numerical methods[4–8, 14–16], composite fermions[17–22] and Lieb-Schultz-Mattis type constraints.[23] On the other hand, the fundamental question regarding the influence of lattice parameters on the onset of topological phase transitions (TPTs) in IHCI and FHCI has received significantly less attention.[24–26] The complexity of the Hofstadter spectrum and the finite bandwidth of Chern bands that reflects their dependence on the lattice parameters and on the intra-cell magnetic flux appears to stand in the way of an overarching understanding of lattice-tuned phase transitions, which are distinct from Landau level plateau transitions tuned by the magnetic field.[27, 28]

In this paper we shed new light on TPTs in IHCI and FHCI by providing a classification of their quantum critical points and presenting a physical mechanism that explains the onset of TPTs obtained by tuning lattice parameters in the presence of a fixed background magnetic field. Numerical studies[24, 26] strongly support the existence of continuous phase transitions tuned the amplitude of a square lattice weak potential projected on the lowest Landau level. The approach undertaken in this work, on the other hand, begins with an effective tight-binding description (i.e. “strong” potential) of a honeycomb superlattice where the magnetic field is incorporated by a Peirls substitution and discusses topological transitions tuned by hopping amplitudes of the lattice. The realization of graphene superlattices via nanolithog-

raphy [29–34] not only provides a motivation for this study but also offers a promising platform to test these ideas.

We now state the main results of the paper: (1) We show that hopping-tuned TPTs on the honeycomb lattice in the presence of a fixed rational intra-cell magnetic flux $\phi = (p/q)\phi_0$ are characterized by q Dirac fermions (DFs) located in high-symmetry momenta of the magnetic Brillouin zone. The number of DF flavors and their momentum space distribution are derived analytically from the properties of a non-trivial function that implicitly sets the momentum dependence of *all* the Chern bands of the spectrum. (2) We establish a surprising connection between van Hove singularities[35] and the onset of TPTs near charge neutrality. (3) After establishing these non-perturbative results for non-interacting IHCI transitions, we further extend the analysis to hopping-tuned FHCI transitions described by composite fermions.[17–22]

Our setting is a honeycomb superlattice in a external perpendicular magnetic field, $B = \partial_x A_y - \partial_y A_x$, described by the single-particle nearest neighbor effective Hamiltonian

$$H = - \sum_{\langle \mathbf{r}, \mathbf{r}' \rangle} t_{\mathbf{r}, \mathbf{r}'} e^{i \frac{2\pi}{\phi_0} \int_{\mathbf{r}}^{\mathbf{r}'} d\mathbf{x} \cdot \mathbf{A}(\mathbf{x})} a_{\mathbf{r}}^\dagger b_{\mathbf{r}'} + \text{H.c.} \quad (1)$$

Here, $a_{\mathbf{r}}^\dagger = a_{m,n}^\dagger$ and $b_{\mathbf{r}}^\dagger = b_{m,n}^\dagger$ are spin polarized fermionic creation operators on the two sublattices, $\mathbf{r} = m\mathbf{a}_1 + n\mathbf{a}_2$, $m, n \in \mathbb{Z}$ is the lattice vector with basis vectors $\mathbf{a}_1 = a(3/2, -\sqrt{3}/2)$ and $\mathbf{a}_2 = a(3/2, \sqrt{3}/2)$, and $t_{\mathbf{r}, \mathbf{r}'} = \{t_1, t_2, t_3\}$ are nearest neighbor real hopping elements, as shown in Fig.1(a).

We work in the gauge $\mathbf{A} = \hat{y}(x + \sqrt{3}y)B$ with rational flux $\phi = B \frac{\sqrt{3}}{2} a^2 = (p/q)\phi_0$ ($p, q \in \mathbb{Z}_+$ and coprime) per unit cell, and discuss TPTs within the single particle Chern bands of the Hamiltonian (1). For that we introduce the magnetic unit cell containing $2q$ inequivalent sites with corresponding lattice translation vectors $\{\tilde{\mathbf{a}}_1, \tilde{\mathbf{a}}_2\} = \{\mathbf{a}_1, q\mathbf{a}_2\}$. Then the Hamiltonian in reciprocal space is directly expressed as [36] $H = - \sum_{\mathbf{k} \in \text{MBZ}} \psi_{\mathbf{k}}^\dagger \tau_1 \otimes h_{\mathbf{k}} \psi_{\mathbf{k}}$, where $\mathbf{k} = (k_1, k_2) \equiv k_1 \tilde{\mathbf{g}}_1 + k_2 \tilde{\mathbf{g}}_2$ is the momenta inside the magnetic Brillouin

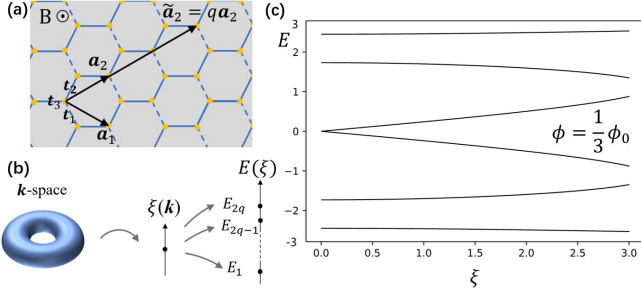


FIG. 1. (a) Honeycomb superlattice with lattice constant in the nms. (b) Momentum dependence on the Thouless function ξ . (c) Spectrum as function of ξ for $\phi = (1/3)\phi_0$.

zone (MBZ), $k_i \in [-\pi, \pi)$, with $\tilde{\mathbf{g}}_1 = 1/(3a)\hat{x} - 1/(\sqrt{3}a)\hat{y}$ and $\tilde{\mathbf{g}}_2 = 1/(3qa)\hat{x} + 1/(\sqrt{3}qa)\hat{y}$ being the reciprocal vectors.

In the following we seek a non-perturbative understanding of how the energy bands depend on momentum as well as the hopping parameters, beyond the isotropic case.[37–39] For that, we establish the general form of the spectral function $\mathcal{P}(E) = \det(EI - H)$,

$$\mathcal{P}(E) = \sum_{n=1}^q a_n(\{t_i\}) E^{2n} - \xi^2(\{t_i\}, k_1, k_2), \quad (2a)$$

$$\xi(\{t_i\}, k_1, k_2) = |t_1^q e^{iqk_1 - \pi(q-1)} + t_2^q e^{ik_2} + t_3^q| > 0. \quad (2b)$$

Eq.(2) encodes a remarkable property of the Hofstadter spectrum, originally noticed by Thouless in a different context[40] (see also[37]), namely, that the momentum dependence of the bands is entirely “compressed” in a single function $\xi(\mathbf{k})$, i.e. $E_\alpha(\mathbf{k}) = E_\alpha(\xi(\mathbf{k}))$ for $\alpha = 1, \dots, 2q$. This property is illustrated in Figs. 1(b) and 1(c), where the energy bands are plotted in terms of the “Thouless function” ξ . We further notice that this function is directly related to the graphene band structure[41] subject to replacement $(k_1, k_2) \rightarrow (qk_1 - \pi(q-1), k_2)$ and $\{t_i\} \rightarrow \{t_i^q\}$.

IHCI transitions - We will now derive exact results, based on the properties of the Thouless function, that lead to a classification of TPTs in the parameter space (t_1, t_2, t_3) . On general grounds, consider a phase transition tuned by the hopping parameters where two Chern bands touch at (ξ_F, E_F) , where $E_F \neq 0$ is the Fermi energy. ($E_F = 0$ band touchings will be discussed shortly after.) Let $\mathcal{P}(E) = \sum_{n=1}^q c_n (E^2 - E_F^2)^n - (\xi^2 - \xi_F^2)$ be the Taylor expansion of the characteristic polynomial Eq.(2a) about $E = E_F$, where $\xi_F \equiv \mathcal{P}(E_F) \neq 0$ and c_n are coefficients readily determined. The even powers of E in Eq.(2a) reflect the spectral particle-hole symmetry, viz. non-zero energy eigenvalues form symmetric pairs $\pm E$. Therefore, since $\pm E_F \neq 0$ are doubly degenerate roots of the characteristic polynomial, it follows that $\mathcal{P}(E) = (E^2 - E_F^2)^2 g(E)$, where $g(E)$ is a polynomial

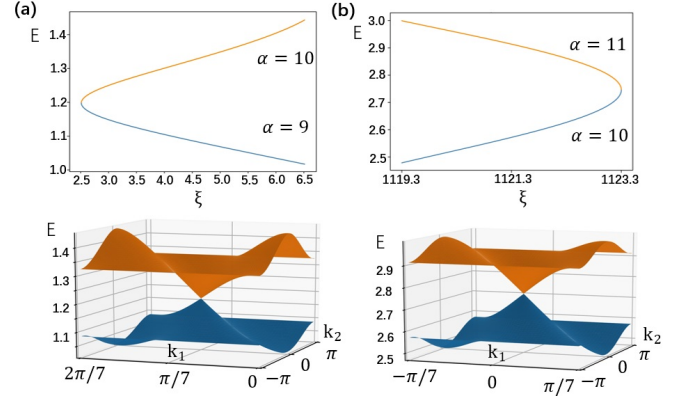


FIG. 2. TPTs of the $\phi = (1/7)\phi_0$ lattice (α denotes band index). (a) At $(t_1, t_2, t_3) = (1.24, 1, 1)$, 7 Dirac cones (only one shown) form at $\mathbf{k}_{min}^{(n)} = (-\pi/7 + 2\pi n/7, 0)$, $n = 0, \dots, 6$. (b) At $(t_1, t_2, t_3) = (2.73, 1, 1)$, 7 Dirac cones (only one shown) form at $\mathbf{k}_{max}^{(n)} = (2\pi n/7, 0)$, $n = 0, \dots, 6$.

in E of order $2(q-2)$. This readily implies the coefficient $c_1 = 0$, leading to the relation between the Thouless function and the energy of the bands in the vicinity of the touching point,

$$\xi \approx \xi_F + 2c_2 E_F^2 \xi_F^{-1} (E - E_F)^2, \quad \xi_F \neq 0. \quad (3)$$

Consequently, the sign of c_2 determines whether the transition occurs through the minimum ($\xi_F = \xi_{min}$) or maximum ($\xi_F = \xi_{max}$) of the Thouless function. Furthermore, upon expanding near the extremal points, i.e., $\xi_{min(max)}(\mathbf{k}) \approx \xi_F + \frac{a}{2} (\mathbf{k} - \mathbf{k}_{min(max)})^2$ [with $a > 0 (< 0)$], and substituting onto Eq.(3), we obtain the dispersion

$$E - E_F = \pm v_F^* |\mathbf{k} - \mathbf{k}_{min(max)}|, \quad v_F^* = (a\xi_F/4c_2 E_F^2)^{1/2}, \quad (4)$$

characteristic of a Dirac cone centered at $\mathbf{k}_{min(max)}$. Fig.2 presents two IHCI TPTs for $\phi = \phi_0/7$ that confirm the general behavior described in Eq.(3) and Eq.(4). The considerations above, therefore, uncover a non-trivial link between the classification of critical points and the global properties of the Thouless function, which we now address in detail.

Eq.(2a) establishes a one-to-one correspondence between the zero modes of ξ and band touchings at $E = 0$, which are described by the low energy relation $E \approx \pm \xi/a_1^{1/2}$. Then, we directly determine from Eq.(2b) that the band structure with isotropic hoppings supports $2q$ Dirac touchings at $E = 0$ [42–44] located at

$$\mathbf{K}_{\pm}^{(n)} = \left(\pm \frac{2\pi}{3q} + \frac{\pi}{q} (2n + q - 1), \mp \frac{2\pi}{3} \right) \quad (5)$$

$n = 0, \dots, q-1$, and furthermore, that these band touchings persist as long as

$$\left| \left| \frac{t_1}{t_2} \right|^q - 1 \right| \leq \left| \frac{t_3}{t_2} \right|^q \leq \left| \left| \frac{t_1}{t_2} \right|^q + 1 \right|. \quad (6)$$

Eq.(6), with $q = 1$, reproduces the stability of the pair of Dirac cones in graphene bands.[45, 46] The global properties of the Thouless function lead to a remarkably simple classification of critical points:

(I) When condition (6) holds, $\xi \geq 0$ and there are $2q$ Dirac band touchings at $(\xi = 0, E = 0)$. Furthermore, TPTs at non-zero Fermi energy occur through q Dirac band touchings located at $\mathbf{k}_{max}^{(n)} = (\pi(2n + q - 1)/q, 0)$, $n = 0, \dots, q - 1$, where $\xi(\mathbf{k}_{max}^{(n)}) = \xi_{max}$.

(II) Outside the parameter space (6), $\xi > 0$ and the spectrum has a gap at half filling. The $2q$ zero modes of ξ merge pairwise forming q quadratic minima at one of the saddle points $\mathbf{M}_1^{(n)} = (\pi(2n + q - 1)/q, -\pi)$, $\mathbf{M}_2^{(n)} = (-\pi/q + \pi(2n + q - 1)/q, 0)$ or $\mathbf{M}_3^{(n)} = (-\pi/q + \pi(2n + q - 1)/q, -\pi)$, for $n = 0, \dots, q - 1$. Then, $E_F \neq 0$ critical points are realized by q Dirac band touchings located either at the minima or at the maxima of ξ . Taking, for concreteness,

$$t_2 = t_3 = 1, \quad t_1 > 0, \quad (7)$$

leads to case (I) for $0 < t_1 \leq 2^{1/q}$ and case (II) when $t_1 > 2^{1/q}$, where the q degenerate minima of ξ are located at $\mathbf{k}_{min}^{(n)} = \mathbf{M}_2^{(n)}$, for $n = 0, \dots, q - 1$. The TPTs of Fig.2 correspond to case (II) with the hopping parameters Eq.(7).

(III) The q Dirac fermions at quantum criticality are constrained by the action of magnetic translation, under which $(k_1, k_2) \rightarrow (k_1 + \frac{2\pi}{q}, k_2)$, and they account for the transfer of Chern number $\Delta C = \pm q$ between the bands, according to standard parity anomaly considerations.[47] We have performed extensive numerical calculations that confirm the properties (I), (II) and (III).

Having classified the IHCI critical points, we now address the *mechanism* underlying such phenomenon. Remarkably, we argue and numerically demonstrate that TPTs naturally occur when Chern bands cross the energy scales associated with the vHs of the DF band in the center of the spectrum. In what follows, we shall demonstrate this striking phenomenon using the hopping t_1 in (7) as the tuning parameter.

To unearth the connection between vHs and TPTs, we consider two Hofstadter systems, denoted A and B, with fluxes $\phi_A = p_A/q_A$ and $\phi_B = p_B/q_B$ [henceforth we set $h = e = 1$ such that $\phi_0 = 1$ and $\phi \sim \phi \bmod (1)$]. Furthermore, we impose upon these systems the conditions (a) $|(\phi_A - \phi_B)/\phi_0| \ll 1$ and (b) $q_B \gtrsim q_A$, with the goal of addressing the TPTs of system B using the system A as a reference. For that, we initially consider system A with $t_i = 1$, which displays $2q_A$ DFs at half-filling with low-energy dispersion $E_{Dirac,A}(\mathbf{k}) \approx \xi_A(t_i = 1; \mathbf{k} - \mathbf{K}_{\pm})/a_1^{1/2}$; see Eq.(5). Due to particle-hole symmetry, we restrict the following discussion to $E \geq 0$. General considerations give the characteristic Dirac-like density of states (DOS) $D_A \propto E$ near charge neutrality, which is cut off by the van Hove singularity energy E_{vHs}^A

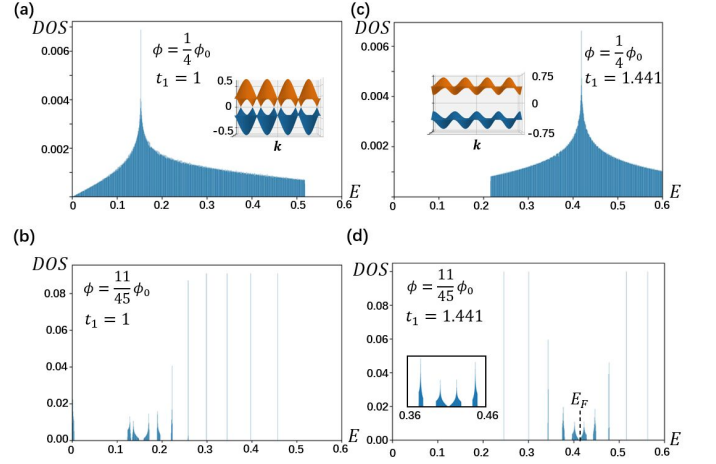


FIG. 3. (a) DOS of the Dirac center band at $\phi_A = (1/4)\phi_0$ and $(t_1, t_2, t_3) = (1, 1, 1)$. Inset shows the 8 gapless Dirac cones, whose locations are given by Eq.(5). (b) DOS at $\phi_B = (11/45)\phi_0$ and $(t_1, t_2, t_3) = (1, 1, 1)$ reflecting the reconstruction of the Dirac band in (a). (c) DOS of the Dirac center band at $\phi_A = (1/4)\phi_0$ and $(t_1, t_2, t_3) = (1.441, 1, 1)$. Inset shows the 8 gapped Dirac cones. The gap-opening threshold is $t_1 = 2^{1/4} \approx 1.19$. (d) DOS at $\phi_B = (11/45)\phi_0$ and $(t_1, t_2, t_3) = (1.441, 1, 1)$ reflecting the reconstruction of the gapped Dirac band in (c). The inset shows the emergence of Dirac fermions at the critical point.

that distinguishes electron-like from the hole-like states. Fig.3(a) displays the DOS (for $E \geq 0$) of the band near charge neutrality for $\phi_A = 1/4$, which supports 8 Dirac fermions and has $E_{vHs}^A \approx 0.15$. Notice that, compared to the graphene bands[41], the magnetic field pushes the vHs substantially closer to the charge neutrality point due to the splitting of the graphene spectrum into $2q_A$ bands.

Furthermore, condition (a) ensures the spectrum of B near half-filling can be understood as the response of the DF band of A to a weak “residual” magnetic field, which is expected to give rise to relativistic-like (non-relativistic-like) Landau levels for $E \lesssim (\gtrsim) E_{vHs}^A$. However, the Chern bands of B in the proximity to E_{vHs}^A deviate substantially from the Landau level behavior. This is illustrated in Fig.3(b) for the B system with $\phi_B = 11/45 \approx 1/4$, where the said bands show more pronounced bandwidths and narrower gaps in comparison with others. It naturally follows that the dependence of E_{vHs}^A as t_1 changes away from the isotropic point, as shown in Fig.4, steers the “vHs-Chern bands” present in the spectrum of the B system and gives rise to a sequence of phase transitions. This mechanism is one of the main aspects of this work.

The implicit momentum dependence of the band energies $E_\alpha(\mathbf{k}) = E_\alpha(\xi(\mathbf{k}))$ establishes that the vHs occur in \mathbf{k} space at saddle points of the Thouless function. Direct calculation shows that ξ is degenerate on all the saddle points $\mathbf{M}_{1,2,3}^{(n)}$ when $t_1 = 1$ and, furthermore, that

the degeneracy is partially broken for $t_1 \neq 1$. [36] For $1 < t_1 < 2^{1/q}$ (case (I) above), we find that the vHs splits into a large peak at $E_{\text{vHs},1}^A$ [due to $\xi(\mathbf{M}_1^{(n)}) = \xi(\mathbf{M}_3^{(n)})$], and a small peak at $E_{\text{vHs},2}^A$ [due to $\xi(\mathbf{M}_2^{(n)})$]. The lower vHs peak disappears in the lower band edge, for $t_1 > 2^{1/q}$ (case (II) above), where an energy gap forms, which is shown in Fig.3(c). Moreover, Fig.3(d) (see inset) displays the onset of a phase transition as the result of the vHs-Chern bands being steered by the $E_{\text{vHs},1}^A$ energy scale.

A general depiction of the remarkable relationship between the vHs of system A and TPTs in the vHs-Chern bands of B is shown in Fig.4. The energy scales $E_{\text{vHs},1}^A$ and $E_{\text{vHs},2}^A$, are shown, respectively, by the solid green and purple curves in the interval $t_1 \geq 1$. In addition, the Dirac energies $E_{\text{Dirac},A}(\mathbf{M}_1^{(n)})$ and $E_{\text{Dirac},A}(\mathbf{M}_2^{(n)})$, which are represented in Fig.4 by dashed green and purple curves, set upper bounds on the vHs energies evaluated at the respective saddle points. It is noteworthy that $E_{\text{vHs},1}^A$ and $E_{\text{vHs},2}^A$ track the center of the highest spectral weight of the vHs-Chern bands of B and, as this process unfolds, the bands of B are steered towards the two vHs of A. This results in a transfer of spectral weight between the vHs-Chern bands that accounts for observed phase transitions. Furthermore, according to the classification of quantum critical points discussed above, each of these critical points (marked by vertical arrows) realizes q_B Dirac points located at the global minima or maxima of the Thouless function, where a transfer of Chern number $|C| = q_B$ occurs between the bands. Indeed, we have numerically confirmed that the transitions shown in Fig.4 indeed take place through 45 Dirac fermions. Moreover, we have found that the vHs steering mechanism is ubiquitous and applies to Chern bands associated with magnetic fluxes other than the ones discussed here.

FHCI transitions – The analysis of TPTs in the context of non-interacting IHCI also lead to non-trivial implications about FHCI transitions tuned by the hopping parameters in partially filled Chern bands. We approach this question within the standard representation of an FHCI with Hall conductance $\sigma_{xy}(C) = C/(2C+1)$ in terms of a composite fermion system [17, 18, 48] in an IHCI with $\sigma_{xy}^{CF} = C$ [19, 20], which is subject to a mean field residual flux

$$\phi_{CF} = \phi - \phi_{CS}, \quad (8)$$

where $\phi = B \frac{\sqrt{3}}{2} a^2$ and $\phi_{CS} = 4n$ are, respectively, the intra-cell fluxes due to the external magnetic field and the Chern-Simons gauge field at lattice filling n , for $0 \leq n \leq 1$ (the factor of 4 accounts for 2 attached flux quanta and 2 sites per unit cell). Then, a TPT at fixed B and n between FHCIs with $\sigma_{xy}(C_1) = C_1/(2C_1+1)$ and $\sigma_{xy}(C_2) = C_2/(2C_2+1)$ can be effectively described by a $C_1 \rightarrow C_2$ composite fermion transition subject to the constraint $|C_2 - C_1| = q_{cf}$ (recall property (III)), where $\phi_{CF} = p_{cf}/q_{cf}$ is the flux of the composite fermion

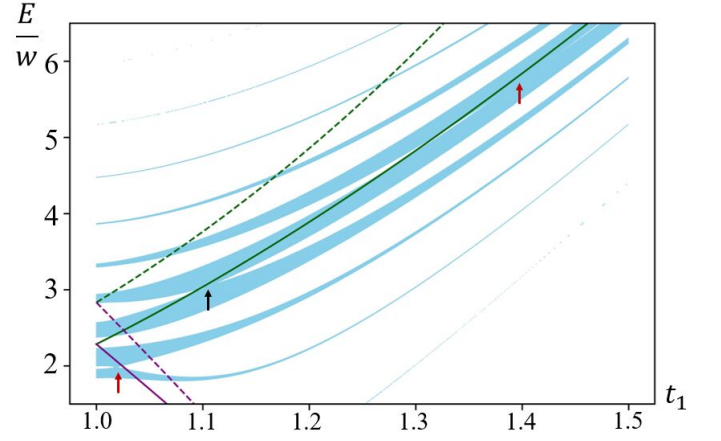


FIG. 4. TPTs of system B ($\phi_B = 11/45$) steered by the van Hove singularities of system A ($\phi_A = 1/4$). All energies are rescaled by the average band separation w of the B system with $t_1 = 1$. $E_{\text{vHs},1}^A$ and $E_{\text{vHs},2}^A$ are represented, respectively, by solid green and purple lines. Dashed green and purple lines represent $E_{\text{Dirac},A} = \xi/\sqrt{a_1}$ evaluated, respectively, at the saddle points \mathbf{M}_1 and \mathbf{M}_2 of ξ . The composite fermion phase transitions at $n = 47/90$ and $n = 50/90$ are marked by vertical red arrows.

state. Furthermore, Eq.(8) imposes a second constraint that allows the identification of candidate TPTs between Abelian FHCI states, which can be further studied by other methods. In closing we present two such candidate FHCI transitions realized in the composite fermion state with $\phi_{CF} = 11/45$, which are shown by vertical red arrows in Fig.4. The first TPT is observed at $t_1 \approx 1.02$ at filling $n = 47/90$ and external flux $\phi = 1/3$, which is associated with $E_{\text{vHs},2}^A$. Upon numerical calculation of the composite fermion Chern numbers, we determine that this is a transition between FHCIs with $\sigma_{xy}(37) = 37/75$ and $\sigma_{xy}(-8) = 8/15$. On the second transition, which happens at $t_1 \approx 1.44$ with filling $n = 50/90 = 5/9$ and external flux $\phi = 7/15$, the Hall conductance jumps from $\sigma_{xy}(25) = 25/51$ to $\sigma_{xy}(-20) = 20/39$. We point the reader to the SM [36] for another example of FHCI transition.

In summary, we have proposed an analytical framework to classify multi-flavor Dirac fermion critical points describing hopping-tuned topological phase transitions of integer and fractional Hofstadter-Chern insulators in honeycomb superlattices. Our classification sets firm constraints on the number of Dirac flavors as well as their momentum space distribution in terms of the hopping parameters, the magnetic flux per unit cell and the electron density. Such critical points realize large transfers of Chern number across the phase transition, which can be detected via conductivity measurements. We have identified a series of topological phase transitions that can be explained by the non-trivial response of Chern bands to van Hove singularities near charge neutrality. These results, which were derived from the identification

of global properties of the Chern bands, lead to a new understanding of quantum critical phenomena resulting from the interplay of magnetic field and van Hove singularities. This work opens many interesting directions to study quantum critical phenomena in superlattices. Besides nanopatterned graphene superlattices [29–34] that served as a motivation for this work, van der Waals heterostructures in external magnetic field [9–11, 13] provide promising platforms to realize topological quantum criticality via strain induced tuning of the effective hopping parameters. Also, the interplay of magnetic field and higher order van Hove singularities [49, 50] can potentially provide even richer critical phenomena. We leave these open questions to future work.

Acknowledgements— We acknowledge useful discussions with Claudio Chamon, Ankur Das, Ribhu Kaul, Ganpathy Murthy and Raman Sohal. Part of this work was performed at the Aspen Center for Physics, which is supported by National Science Foundation grant PHY-1607611. LHS is supported by a faculty startup at Emory University.

-
- [1] D. J. Thouless, M. Kohmoto, M. P. Nightingale, and M. den Nijs, *Phys. Rev. Lett.* **49**, 405 (1982).
 - [2] F. D. M. Haldane, *Phys. Rev. Lett.* **61**, 2015 (1988).
 - [3] D. R. Hofstadter, *Phys. Rev. B* **14**, 2239 (1976).
 - [4] T. Neupert, L. Santos, C. Chamon, and C. Mudry, *Phys. Rev. Lett.* **106**, 236804 (2011).
 - [5] D. N. Sheng, Z.-C. Gu, K. Sun, and L. Sheng, *Nature Communications* **2**, 389 EP (2011).
 - [6] E. Tang, J.-W. Mei, and X.-G. Wen, *Phys. Rev. Lett.* **106**, 236802 (2011).
 - [7] K. Sun, Z. Gu, H. Katsura, and S. Das Sarma, *Phys. Rev. Lett.* **106**, 236803 (2011).
 - [8] N. Regnault and B. A. Bernevig, *Phys. Rev. X* **1**, 021014 (2011).
 - [9] C. R. Dean, L. Wang, P. Maher, C. Forsythe, F. Ghahari, Y. Gao, J. Katoch, M. Ishigami, P. Moon, M. Koshino, T. Taniguchi, K. Watanabe, K. L. Shepard, J. Hone, and P. Kim, *Nature* **497**, 598 EP (2013).
 - [10] L. A. Ponomarenko, R. V. Gorbachev, G. L. Yu, D. C. Elias, R. Jalil, A. A. Patel, A. Mishchenko, A. S. Mayorov, C. R. Woods, J. R. Wallbank, M. Mucha-Kruczynski, B. A. Piot, M. Potemski, I. V. Grigorieva, K. S. Novoselov, F. Guinea, V. I. Fal'ko, and A. K. Geim, *Nature* **497**, 594 EP (2013).
 - [11] B. Hunt, J. D. Sanchez-Yamagishi, A. F. Young, M. Yankowitz, B. J. LeRoy, K. Watanabe, T. Taniguchi, P. Moon, M. Koshino, P. Jarillo-Herrero, and R. C. Ashoori, *Science* **340**, 1427 (2013).
 - [12] C. Forsythe, X. Zhou, K. Watanabe, T. Taniguchi, A. Pasupathy, P. Moon, M. Koshino, P. Kim, and C. R. Dean, *Nature nanotechnology* **13**, 566 (2018).
 - [13] E. M. Spanton, A. A. Zibrov, H. Zhou, T. Taniguchi, K. Watanabe, M. P. Zaletel, and A. F. Young, *Science* **360**, 62 (2018).
 - [14] Z. Liu, E. J. Bergholtz, H. Fan, and A. M. Läuchli, *Phys. Rev. Lett.* **109**, 186805 (2012).
 - [15] Y.-L. Wu, B. A. Bernevig, and N. Regnault, *Phys. Rev. B* **85**, 075116 (2012).
 - [16] A. M. Läuchli, Z. Liu, E. J. Bergholtz, and R. Moessner, *Phys. Rev. Lett.* **111**, 126802 (2013).
 - [17] J. K. Jain, *Phys. Rev. Lett.* **63**, 199 (1989).
 - [18] A. López and E. Fradkin, *Phys. Rev. B* **44**, 5246 (1991).
 - [19] A. Kol and N. Read, *Phys. Rev. B* **48**, 8890 (1993).
 - [20] G. Möller and N. R. Cooper, *Phys. Rev. Lett.* **115**, 126401 (2015).
 - [21] G. Murthy and R. Shankar, *Phys. Rev. B* **86**, 195146 (2012).
 - [22] R. Sohal, L. H. Santos, and E. Fradkin, *Phys. Rev. B* **97**, 125131 (2018).
 - [23] Y.-M. Lu, Y. Ran, and M. Oshikawa, *Annals of Physics* **413**, 168060 (2020).
 - [24] D. Pfannkuche and A. H. MacDonald, *Physical Review B* **56**, R7100 (1997).
 - [25] M. Sato, D. Tobe, and M. Kohmoto, *Phys. Rev. B* **78**, 235322 (2008).
 - [26] J. Y. Lee, C. Wang, M. P. Zaletel, A. Vishwanath, and Y.-C. He, *Phys. Rev. X* **8**, 031015 (2018).
 - [27] J. K. Jain, S. A. Kivelson, and N. Trivedi, *Phys. Rev. Lett.* **64**, 1297 (1990).
 - [28] S. Kivelson, D.-H. Lee, and S.-C. Zhang, *Phys. Rev. B* **46**, 2223 (1992).
 - [29] M. Gibertini, A. Singha, V. Pellegrini, M. Polini, G. Vignale, A. Pinczuk, L. N. Pfeiffer, and K. W. West, *Phys. Rev. B* **79**, 241406 (2009).
 - [30] A. Singha, M. Gibertini, B. Karmakar, S. Yuan, M. Polini, G. Vignale, M. I. Katsnelson, A. Pinczuk, L. N. Pfeiffer, K. W. West, and V. Pellegrini, *Science* **332**, 1176 (2011).
 - [31] A. Soibel, U. Meirav, D. Mahalu, and H. Shtrikman, *Semiconductor Science and Technology* **11**, 1756 (1996).
 - [32] L. Nádvorník, M. Orlita, N. A. Goncharuk, L. Smrčka, V. Novák, V. Jurka, K. Hruška, Z. Výborný, Z. R. Wasilewski, M. Potemski, and K. Výborný, *New Journal of Physics* **14**, 053002 (2012).
 - [33] S. Wang, D. Scarabelli, Y. Y. Kuznetsova, S. J. Wind, A. Pinczuk, V. Pellegrini, M. J. Manfra, G. C. Gardner, L. N. Pfeiffer, and K. W. West, *Applied Physics Letters* **109**, 113101 (2016).
 - [34] S. Wang, D. Scarabelli, L. Du, Y. Y. Kuznetsova, L. N. Pfeiffer, K. W. West, G. C. Gardner, M. J. Manfra, V. Pellegrini, S. J. Wind, and A. Pinczuk, *Nature Nanotechnology* **13**, 29 (2018).
 - [35] L. Van Hove, *Phys. Rev.* **89**, 1189 (1953).
 - [36] See Supplemental Material for details on (i) k -space Hamiltonian, (ii) properties of the Thouless function, (iii) further examples of the relation between the vHs energy scale and topological phase transitions.
 - [37] R. Rammal, *Journal de Physique* **46**, 1345 (1985).
 - [38] B. Andrei Bernevig, T. L. Hughes, S.-c. Zhang, H.-d. Chen, and C. Wu, *International Journal of Modern Physics B* **20**, 3257 (2006).
 - [39] A. Agazzi, J.-P. Eckmann, and G. M. Graf, *Journal of Statistical Physics* **156**, 417 (2014).
 - [40] D. J. Thouless, *Phys. Rev. B* **28**, 4272 (1983).
 - [41] A. H. Castro Neto, F. Guinea, N. M. R. Peres, K. S. Novoselov, and A. K. Geim, *Rev. Mod. Phys.* **81**, 109 (2009).
 - [42] J.-W. Rhim and K. Park, *Phys. Rev. B* **86**, 235411 (2012).

- [43] I. N. Karnaukhov, Physics Letters A **383**, 2114 (2019).
 [44] A. Das, R. K. Kaul, and G. Murthy, Phys. Rev. B **101**, 165416 (2020).
 [45] Y. Hasegawa, R. Konno, H. Nakano, and M. Kohmoto, Phys. Rev. B **74**, 033413 (2006).
 [46] B. Wunsch, F. Guinea, and F. Sols, New Journal of Physics **10**, 103027 (2008).
 [47] A. N. Redlich, Phys. Rev. Lett. **52**, 18 (1984).
 [48] B. I. Halperin, P. A. Lee, and N. Read, Phys. Rev. B **47**, 7312 (1993).
 [49] D. V. Efremov, A. Shtyk, A. W. Rost, C. Chamon, A. P. Mackenzie, and J. J. Betouras, Physical Review Letters **123**, 207202 (2019).
 [50] N. F. Q. Yuan, H. Isobe, and L. Fu, Nature Communications **10**, 5769 (2019).

Supplemental Material

HONEYCOMB HOFSTADTER HAMILTONIAN IN THE MOMENTUM SPACE

In this section we provide details of the momentum space form of the Hamiltonian, which was omitted in the main text. In the gauge $\mathbf{A} = \hat{y}(x + \sqrt{3}y)B$, the real space Hamiltonian

$$H = - \sum_{\langle \mathbf{r}, \mathbf{r}' \rangle} t_{\mathbf{r}, \mathbf{r}'} e^{i \frac{2\pi}{\phi_0} \int_{\mathbf{r}}^{\mathbf{r}'} d\mathbf{x} \cdot \mathbf{A}(\mathbf{x})} a_{\mathbf{r}}^\dagger b_{\mathbf{r}'} + \text{H.c.} \quad (\text{S1})$$

takes the form

$$H = - \sum_{m,n} a_{m,n}^\dagger \left(t_3 + \omega^{-n} t_1 \hat{T}_{\mathbf{a}_1} + \omega^n t_2 \hat{T}_{\mathbf{a}_2} \right) b_{m,n} + \text{H.c.} \quad (\text{S2})$$

where $t_{1,2,3}$ are nearest neighbor real hopping elements shown in Fig.1(a), $\omega = e^{2\pi i \frac{p}{q}}$ and $\hat{T}_{\mathbf{a}_{1,2}}$ are the translation operators on the $\mathbf{a}_{1,2}$ directions, with the lattice constant $a = 1$. The magnetic unit cell is formed by extending the original one q times in the \mathbf{a}_2 direction (see Fig.1(a)), giving rise to an effective tight-binding description with $2q$ sites per magnetic unit cell, $(a_{\mathbf{r}}^s, b_{\mathbf{r}}^s)$, where $s = 0, \dots, q-1$, and translation vectors $\{\tilde{\mathbf{a}}_1, \tilde{\mathbf{a}}_2\} = \{\mathbf{a}_1, q\mathbf{a}_2\}$. Then in momentum space, we readily find

$$H = - \sum_{\mathbf{k} \in \text{MBZ}} \psi_{\mathbf{k}}^\dagger \begin{pmatrix} 0 & h_{\mathbf{k}} \\ h_{\mathbf{k}}^\dagger & 0 \end{pmatrix} \psi_{\mathbf{k}} = - \sum_{\mathbf{k} \in \text{MBZ}} \psi_{\mathbf{k}}^\dagger \tau_1 \otimes h_{\mathbf{k}} \psi_{\mathbf{k}}, \quad (\text{S3})$$

with non-zero matrix elements of the $q \times q$ matrix $h_{\mathbf{k}}$ given by

$$\begin{aligned} (h_{\mathbf{k}})_{ss} &= t_3 + t_1 e^{ik_1} \omega^{-s}, \quad s = 0, \dots, q-1, \\ (h_{\mathbf{k}})_{s,s+1} &= t_2 \omega^s, \quad s = 0, \dots, q-2, \\ (h_{\mathbf{k}})_{q-1,0} &= t_2 \omega^{q-1} e^{ik_2}, \end{aligned} \quad (\text{S4})$$

where $\mathbf{k} = k_1 \tilde{\mathbf{g}}_1 + k_2 \tilde{\mathbf{g}}_2$, with $k_i \in [-\pi, \pi)$, denotes the momenta inside the magnetic Brillouin zone (MBZ) with $\tilde{\mathbf{g}}_1 = \frac{1}{3}\hat{x} - \frac{1}{\sqrt{3}}\hat{y}$ and $\tilde{\mathbf{g}}_2 = \frac{1}{q}(\frac{1}{3}\hat{x} + \frac{1}{\sqrt{3}}\hat{y})$ being the reciprocal vectors in Cartesian coordinates satisfying $\tilde{\mathbf{a}}_i \cdot \tilde{\mathbf{g}}_j = \delta_{ij}$.

PROPERTIES OF THE THOULESS FUNCTION

In this section we provide more detailed analysis of the Thouless function and the constraints imposed upon the Chern bands. As discussed after in the main text, the mapping from the Thouless function $\xi(\{t_i\}, k_1, k_2)$ to the band energies $\{E_\alpha(\xi), \alpha = 1, \dots, 2q\}$ determines the position of the band extremal and saddle points of all bands for the system with arbitrary rational flux $\phi = \frac{p}{q}\phi_0$. We show in Fig.(S1) the extremal and saddle points of $\xi(\{t_i\}, k_1, k_2)$ for $q = 1$ in the two relevant hopping parameter regime $t_2 = t_3 = 1, t_1 < 2$ and $t_1 > 2$. The behavior of the energy bands $E_\alpha(\xi)$ for $q > 1$ can thus be similarly derived upon the appropriate replacement $(k_1, k_2) \rightarrow (qk_1 - \pi(q-1), k_2)$ and $\{t_i\} \rightarrow \{t_i^q\}$. Moreover, due to particle-hole symmetry, we are led to consider only the bands above charge-neutrality and define the band index $\beta \equiv \alpha - q$. Therefore, when $0 < t_1 < 2^{1/q}$, the band minimum (maximum) and maximum (minimum) for β odd (even) occur, respectively at $\xi(\mathbf{k}_{0\pm}^{(n)}) = \xi_{\min} = 0$ and $\xi(\mathbf{k}_{\max}^{(n)}) = \xi_{\max} > 0$, where $\mathbf{k}_{0\pm}^{(n)} = ([\pm \arccos(-t_1^q/2) + \frac{\pi(2n+q-1)}{q}], \pm 2 \arccos(-t_1^q/2))$ and, furthermore, $\mathbf{k}_{\max}^{(n)} = (\pi(2n+q-1)/q, 0)$. When

$t_1 > 2^{1/q}$, $\xi(\mathbf{k}) > 0$ and the minimal of the β -odd bands and the maximal of the β -even bands are fixed in \mathbf{k} -space at the $\mathbf{M}_2^{(n)}$ points. We can further infer (i) that when $t_1 < 2^{\frac{1}{q}}$, the isolated energy bands satisfy $dE/d\xi = 0$ at $\xi_{\min} = 0$ so as to prevent the discontinuity in $\nabla E(\mathbf{k}_{0\pm}^{(n)})$ and (ii) that the $t_1 < 2^{\frac{1}{q}}$ Chern transitions happen at $\xi(\mathbf{k}_{max}^{(n)}) = \xi_{max} = |2 + t_1^q|$, where $|dE/d\xi| \rightarrow \infty$ indicates the presence of q Dirac cones in the points $\mathbf{k}_{max}^{(n)}$ of the magnetic Brillouin zone.

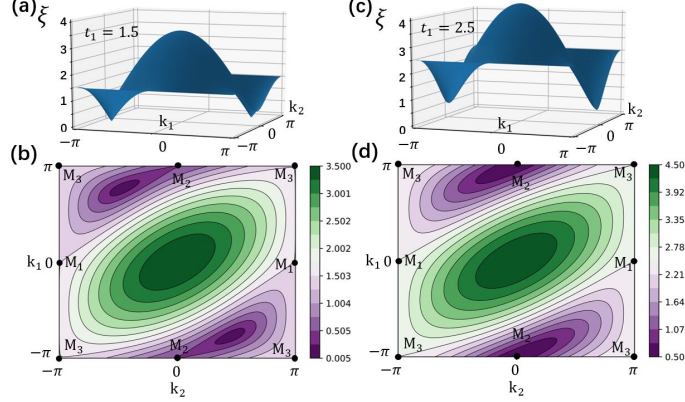


FIG. S1. (a) Thouless's function $\xi(\mathbf{k})$ with $q = 1$ (or equivalently $B = 0$) in the first Brillouin zone at $(t_1, t_2, t_3) = (1.5, 1, 1)$. (b) Contour plot of $\xi(\mathbf{k})$ with $q = 1$ at $(t_1, t_2, t_3) = (1.5, 1, 1)$. $\xi_{\min} = 0$ at the Dirac points $\mathbf{k}_{0-} = -(\arccos(-0.75), 2 \arccos(-0.75)) = (-2.41, 1.44)$ and $\mathbf{k}_{0+} = (2.41, -1.44)$. (c) $\xi(\mathbf{k})$ with $q = 1$ in the first Brillouin zone at $(t_1, t_2, t_3) = (2.5, 1, 1)$. (d) Contour plot of $\xi(\mathbf{k})$ with $q = 1$ at $(t_1, t_2, t_3) = (2.5, 1, 1)$. $\xi_{\min} > 0$ at $\mathbf{M}_2 = (-\pi, 0)$. The behavior for $q > 1$ follows upon replacing $(k_1, k_2) \rightarrow (q k_1 - \pi(q-1), k_2)$ and $\{t_i\} \rightarrow \{t_i^q\}$.

FURTHER EXAMPLES OF THE RELATION BETWEEN VHS AND CHERN TRANSITIONS

In this section we present more examples of the relationship between the vHs of the Dirac fermion band near charge neutrality of system A and the onset of topological phase transitions of system B, where the fluxes of A and B are close to each other. We first recall that the vHs of the $B = 0$ (alternatively, $q = 1$) graphene band splits into two when the hopping parameter t_1 is tuned away from the isotropic lattice $t_1 = t_2 = t_3 = 1$. These vHs energies above charge neutrality, $E_{\text{vHs},1}$ and $E_{\text{vHs},2}$, are given by

$$\begin{aligned} E_{\text{vHs},1} &= E(\mathbf{M}_1) = E(\mathbf{M}_3) = |t_1|, \\ E_{\text{vHs},2} &= E(\mathbf{M}_2) = |2 - t_1| \quad (t_1 < 2). \end{aligned} \quad (\text{S5})$$

If $t_1 > 2$, the Dirac points are gaped and $E_{\text{vHs},2}$ disappears at the lower band edge. As an example, the DOS of the graphene band at different t_1 values is shown in Fig.(S2).

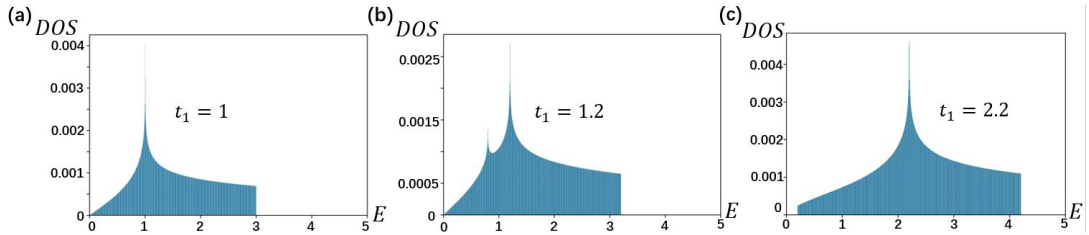


FIG. S2. (a) The $B = 0$ density of states at $(t_1, t_2, t_3) = (1, 1, 1)$. (b) The $B = 0$ density of states at $(t_1, t_2, t_3) = (1.2, 1, 1)$. The vHs split into two for $0 < t_1 < 2$. (c) The $B = 0$ density of states at $(t_1, t_2, t_3) = (2.2, 1, 1)$. The Dirac point is gaped and only $E_{\text{vHs},1}$ is left.

The pattern of vHs splitting due to tuning the hopping parameters also persists to the Chern bands as a consequence of the implicit momentum dependence on Thouless function. In fact, the phenomenon associated with the vHs steering of Chern bands is observed either when $\phi_A = 0$ or when there is a non-trivial flux per unit cell. As argued in the main

text, the following conditions must be satisfied: (a) For the steered system B (which undergoes Chern transitions) and the steering system A (which provides the “background” van Hove singularities), $[(\phi_B - \phi_A)/\phi_0] \ll 1$ and (b) $q_B \gtrsim q_A$. We can understand the phase transitions of the system with $\phi_B = 1/q_B$ (with $q_B > 1$), in terms of the vHs of system A in zero magnetic field. Below, we give concrete examples, one in Fig.(S3), which shows the Chern transitions of the $\phi_B = 1/7$ system and the second one in Fig.(S4), which corresponds to a composite fermion transition at $\phi_{CF} = 1/15$ and $n = 19/30$. In both cases, we see a clear relationship between the onset of phase transitions and the vHs of the $B = 0$ band. Furthermore, we point out that the vHs steering mechanism extends to some degree beyond the Dirac bands near charge neutrality discussed in the main text, as shown in Fig.(S5) for $\phi_A = 1/3$ and $\phi_B = 12/35$, albeit the mechanism for higher bands seems more sensitive to the narrow bandwidth of the Chern bands.

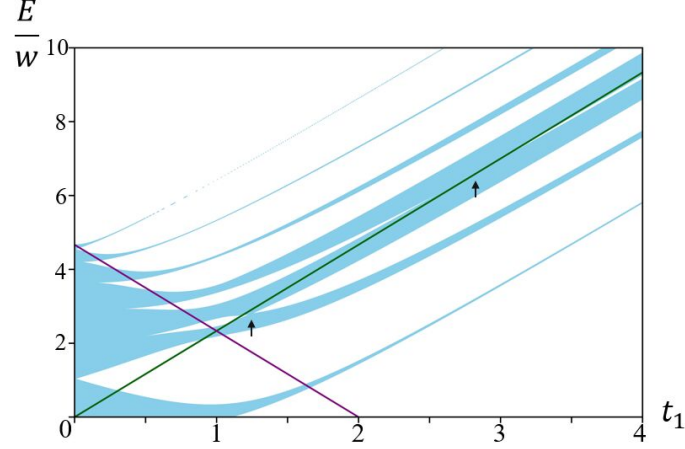


FIG. S3. $\phi = 1/7$ TPTs steered by the $B = 0$ vHs's. The green line shows the van Hove singularity $E_{\text{vHs},1}$ and the purple line showing $E_{\text{vHs},2}$. Here $w = 3/7$ is the average energy separation of bands of the $\phi = 1/7$ spectrum at $t_1 = t_2 = t_3 = 1$. The TPTs are pointed out with black arrows.

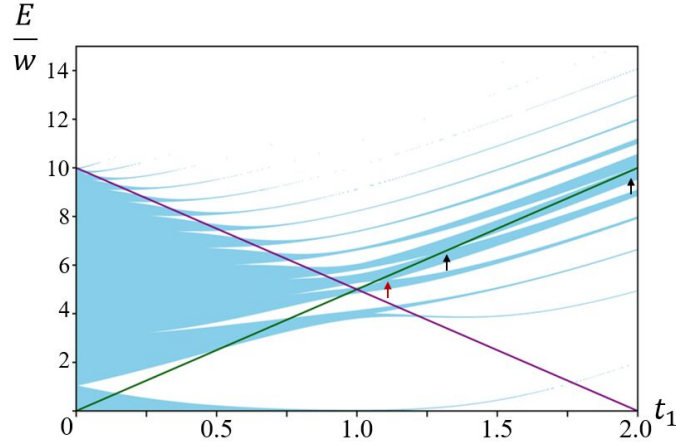


FIG. S4. $\phi_B = 1/15$ TPTs steered by the $B = 0$ vHs's. The green line shows the van Hove singularity $E_{\text{vHs},1}$ and the purple line showing $E_{\text{vHs},2}$. Here $w = 1/5$ is the average energy separation of bands of the $\phi = 1/15$ spectrum at $t_1 = t_2 = t_3 = 1$. The phase transitions are pointed out with vertical arrows, with the red arrow indicating the composite fermion phase transition.

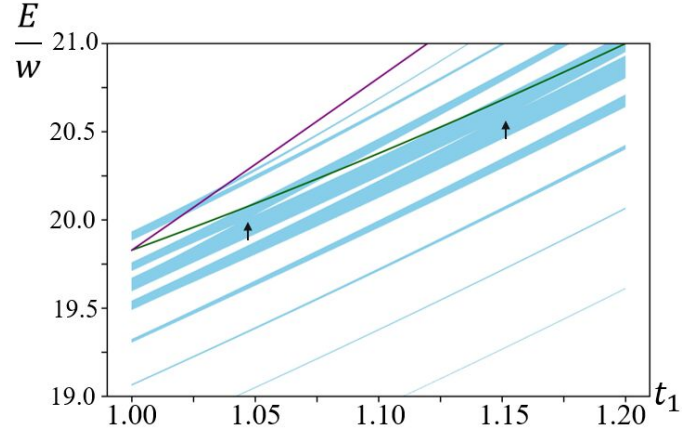


FIG. S5. $\phi_B = 12/35$ TPTs steered by the $\phi_A = 1/3$ vHs's of the 2nd band above charge neutrality as an example of the non-Dirac steering. The green line shows the van Hove singularity $E_{\text{vHs},1}$ and the purple line showing $E_{\text{vHs},2}$. Here $w = 3/35$ is the average energy separation of bands of the $\phi_B = 12/15$ spectrum at $t_1 = t_2 = t_3 = 1$. The TPT is pointed out with the black arrow. Notice that the band touchings deviates a little bit from $E_{\text{vHs},1}$ suggesting a more complex mechanism behind the non-Dirac TPTs, presumably associated with a narrower band.